PHYSICS

Effects of rare-earth magnetism on the superconducting upper critical field in infinite-layer nickelates

Bai Yang Wang[1,2]†*, Tiffany C. Wang[1,3]†*, Yu-Te Hsu[4], Motoki Osada[1,5], Kyuho Lee[1,2], Chunjing Jia[1], Caitlin Duffy[4], Danfeng Li[1], Jennifer Fowlie[1,3], Malcolm R. Beasley[3], Thomas P. Devereaux[1,5], Ian R. Fisher[1,3], Nigel E. Hussey[4,6], Harold Y. Hwang[1,3]*

The search for superconductivity in infinite-layer nickelates was motivated by analogy to the cuprates, and this perspective has framed much of the initial consideration of this material. However, a growing number of studies have highlighted the involvement of rare-earth orbitals; in that context, the consequences of varying the rare-earth element in the superconducting nickelates have been much debated. Here, we show notable differences in the magnitude and anisotropy of the superconducting upper critical field across the La-, Pr-, and Nd-nickelates. These distinctions originate from the 4*f* electron characteristics of the rare-earth ions in the lattice: They are absent for La^{3+}, nonmagnetic for the Pr^{3+} singlet ground state, and magnetic for the Nd^{3+} Kramer's doublet. The unique polar and azimuthal angle-dependent magnetoresistance found in the Nd-nickelates can be understood to arise from the magnetic contribution of the Nd^{3+} 4*f* moments. Such robust and tunable superconductivity suggests potential in future high-field applications.

INTRODUCTION

Following the initial discovery of superconductivity in $Nd_{0.8}Sr_{0.2}NiO_2$ (*1*), the subsequent development of rare-earth (*R*) variants with Pr and La in place of Nd (*2*–*5*) has created an emerging family of superconducting infinite-layer nickelates (Fig. 1A) (*6*–*8*). Unlike the cuprates, with which the nickelates are often compared, *R*-site variations are expected to have appreciable impact beyond ionic size effects. Specifically, rare-earth effects in cuprates are usually overshadowed by the much larger energy scale of superconductivity (*9*, *10*). One exception is in $PrBa_2Cu_3O_{7-\delta}$, where coincidental hybridization between the Pr 4*f* and oxygen 2*p* states is believed to compete with the emergence of superconductivity (*11*). In contrast, in the nickelate superconductors, there is consistent transport, spectroscopic, and theoretical evidence for hybridization between a broad range of *R* 5*d* orbitals and the Ni 3*d* orbitals (*2*–*8*, *12*–*24*). An open question currently under debate is the potential role of the *R* 4*f* electrons (*25*–*28*). Here, we report that the *R*-site directly controls the magnitude and anisotropy of the superconducting upper critical field H_{c2}.

RESULTS

Figure 1 shows a central result motivating this study—that the magnetic field suppression of superconductivity differs widely among *R*-variants, which does not scale with T_{c0}, the superconducting transition temperature in zero external magnetic field. Magnetoresistance measurements up to 35 T of representative (*R*,Sr)NiO_2 (*R* = La, Pr, Nd) samples at optimal doping are shown in Fig. 1 (B to D), for both out-of-plane ($H_\perp$) and in-plane ($H_{||}$) field orientations. The corresponding resistively determined upper critical fields ($H_{c2\perp}$ and $H_{c2||}$; defined as 50% of the normal-state resistivity) are shown (Fig. 1E), where the drastically different scales for H_{c2} are evident.

For a superconductor in the dirty limit, which describes the nickelates (*19*, *29*), the effective Ginzburg-Landau coherence length ξ is the geometric mean of the Pippard coherence length ξ_0 and the mean free path (*30*). Then, as $H_{c2\perp} = \frac{\phi_0}{2\pi\xi^2}\left(1-\frac{T}{T_{c0}}\right)$, $H_{c2\perp} \propto 1/\xi_0 \propto \Delta_0 \propto T_{c0}$. Here, ϕ_0 is the magnetic flux quantum and Δ_0 the superconducting gap. As for $H_{c2||}$, the observed $(1-T/T_{c0})^{1/2}$ temperature dependence indicates dominant paramagnetic depairing near T_{c0} (*19*, *29*). $H_{c2||}$ is also proportional to T_{c0} at temperatures near T_{c0}, described by $-\ln\left(\frac{T}{T_{c0}}\right) = 7\eta(3)\left(\frac{\mu_0 H_{c2||}}{2\pi k_B T_{c0}}\right)^2$ (*31*), where k_B is the Boltzmann constant, μ_0 is the vacuum magnetic permeability, and $\eta(x)$ is the Riemann zeta function. Therefore, we normalize both H_{c2} and *T* by T_{c0} (Fig. 1F) for all samples. We observe a systematic variation in H_{c2}/T_{c0}, which is largest for La-nickelates, somewhat smaller for Pr, and substantially reduced for Nd. Furthermore, this variation between *R*-sites is persistent across the respective superconducting domes via Sr doping (Fig. 1F; see figs. S1 and S2 for complete datasets).

To probe the origin of this large variation in H_{c2}, we measure in detail the magnetoresistance as a function of the polar (θ) and azimuthal (ϕ) angle of the applied magnetic field direction, as illustrated in Fig. 2A. In the normal state, negligible angular dependence is observed for all samples (Fig. 2, C and D). Therefore, we focus on the superconducting transition region with finite sample resistance below the normal-state value. We first present the characteristic features through representative measurements (Fig. 2E; see figs. S3 to

[1]Stanford Institute for Materials and Energy Sciences, SLAC National Accelerator Laboratory, Menlo Park, CA 94025, USA. [2]Department of Physics, Stanford University, Stanford, CA 94305, USA. [3]Department of Applied Physics, Stanford University, Stanford, CA 94305, USA. [4]High Field Magnet Laboratory (HFML-EMFL) and Institute for Molecules and Materials, Radboud University, Toernooiveld 7, 6525 ED Nijmegen, Netherlands. [5]Department of Materials Science and Engineering, Stanford University, Stanford, CA 94305, USA. [6]H. H. Wills Physics Laboratory, University of Bristol, Tyndall Avenue, Bristol BS8 1TL, UK.
*Corresponding author. Email: bwang87@stanford.edu (B.Y.W.); catwang@stanford.edu (T.C.W.); hyhwang@stanford.edu. (H.Y.H.)
†These authors contributed equally to this work.

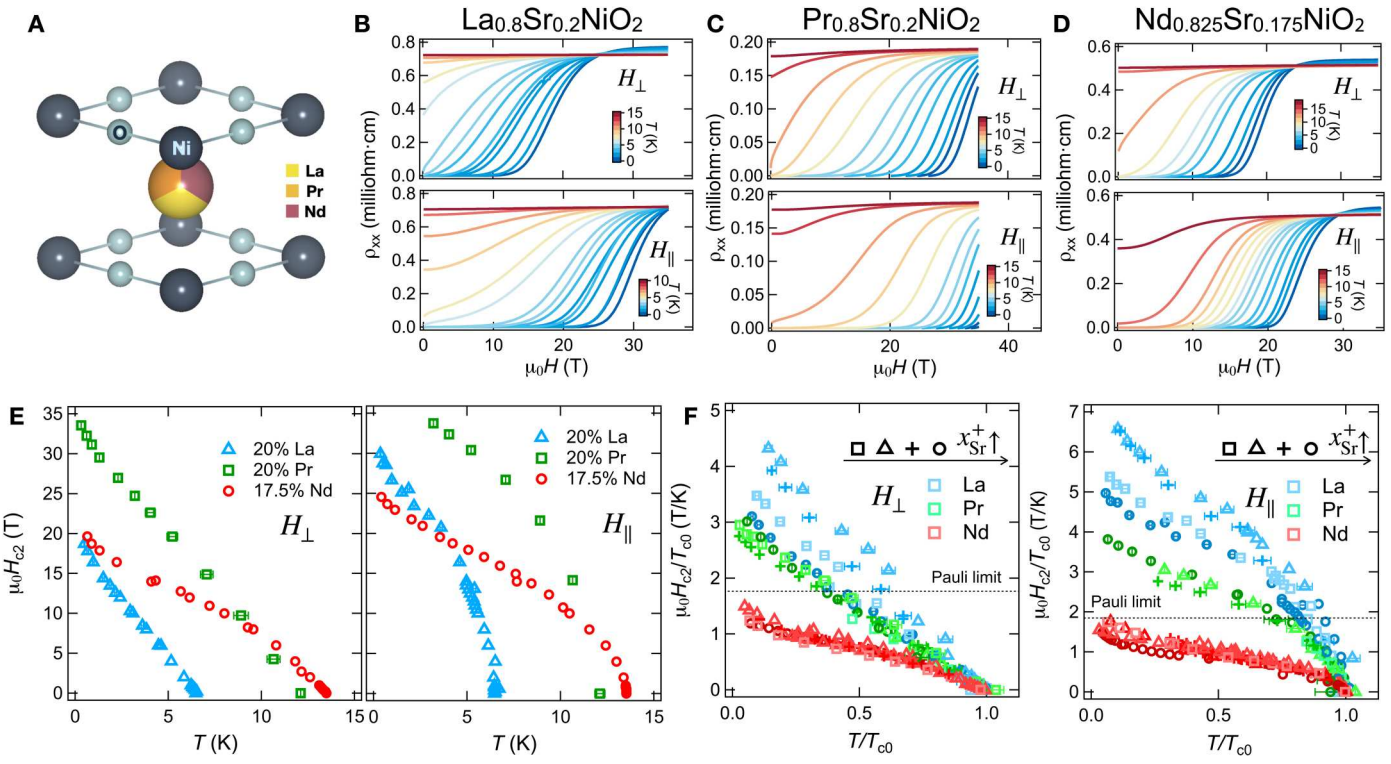

Fig. 1. Structure, magnetotransport, and H_{c2} properties of (R,Sr)NiO_2. (**A**) Schematic unit cell structure of (R,Sr)NiO_2 (R = La, Pr, or Nd; Sr substitution not indicated). (**B** to **D**) Magnetoresistance of representative samples near optimal doping: $La_{0.8}Sr_{0.2}NiO_2$, $Pr_{0.8}Sr_{0.2}NiO_2$, and $Nd_{0.825}Sr_{0.175}NiO_2$ (*20*) respectively, at temperatures ranging from 0.34 to 18 K for out-of-plane ($H_\perp$) and in-plane ($H_{||}$) field orientations. (**E**) Temperature dependence of H_{c2} determined from data shown in (B) to (D). (**F**) Normalized H_{c2}/T_{c0} against reduced temperature T/T_{c0} of $R_{1-x}Sr_xNiO_2$ for $H_\perp$ and $H_{||}$ orientations, respectively. Here, x = 0.15, 0.175, 0.2, and 0.225 (*20*, *29*) for Nd, x = 0.16, 0.18, 0.20, and 0.24 for Pr, and x = 0.15, 0.16, 0.18, and 0.20 for La. The dashed lines indicate the Pauli limit of H_{c2} = 1.86 T_{c0}.

S5 for complete datasets). The La- and Pr-nickelates both show conventional angular dependence; their "∞"-shaped θ-dependence shows that superconductivity is more robust to in-plane magnetic fields than perpendicular fields, as commonly seen in layered superconductors (*32*). Their "figure-of-eight"–shaped ϕ-dependence, arising from vortex motion, also follows previous studies of other type II superconductors (*32*, *33*). In sharp contrast, the Nd-nickelates show qualitatively distinct magnetoresistance. The orientation of the θ-dependence is opposite to that of La-/Pr-nickelates and other layered superconductors, i.e., superconductivity is more suppressed by an in-plane magnetic field, indicating a complete reversal of the superconducting anisotropy. Furthermore, a pronounced clover-leaf ϕ-dependence is observed for Nd. As shown in fig. S6, we can rule out a vortex-related origin of these features.

How can we understand this clear difference between the Nd-nickelates versus the La-/Pr-nickelates? In all cases, the in-plane lattice parameters are clamped to that of the $SrTiO_3$ substrate, while for a specific Sr doping, the c-axis variations reflect the average R-site ionic radii (*1*–*3*): La^{3+} is the largest, ~4.5% larger than the closely similar Pr^{3+} and Nd^{3+} (within 1.5% of each other) (*34*). In addition, the range of the c-axis lattice constant variation of the three R-variants across the superconducting dome substantially overlap. Thus, cation size effects do not seem to account for the unique H_{c2} features in Nd. Rather, the clover-leaf ϕ-dependent magnetoresistance in Nd is more suggestive of a potential role of local magnetic moments, leading to a consideration of the 4*f* electrons and their crystal electric field (CEF) structure.

To examine this, we use theoretical approaches including ab initio density functional theory (DFT) calculations (*35*, *36*), Bader charge analysis (*37*), and symmetry arguments to determine the 4*f* levels split by the tetragonal CEF (see the Supplementary Materials for details). In Fig. 3A, we show the electron density isosurface of the Ni 3*d*, 4*s*, O 2*p*, and R 5*d*, 6*s* orbital electrons within a unit cell where the contours correspond to 2.5% of the maximum electron density. Despite the hybridization, especially between the O 2*p* and Ni 3*d* orbitals, most of the electron density remains within the vicinity of the parent ion. This motivates the use of a point charge approximation in determining the CEF-split 4*f* energy levels, as shown for Pr^{3+} and Nd^{3+} as a function of c-axis lattice constant (Fig. 3, B and C), where the range of experimental values is highlighted by the vertical blue bands and the bulk values are marked by dashed lines (*38*). While La^{3+} has no 4*f* electrons, we find a singlet crystal field ground state for Pr^{3+} that to first order is also nonmagnetic. By contrast, Nd^{3+} has a doublet ground state as expected for a Kramer's ion, making this the lone magnetic R-site ion among the three. Furthermore, by adding an external field term to the CEF perturbation Hamiltonian, we find that the Nd 4*f* moment shows an easy-plane magnetic anisotropy (fig. S7). All of these conclusions are robust to a very large variation of the c-axis lattice parameter, far exceeding the experimentally observed range (Fig. 3).

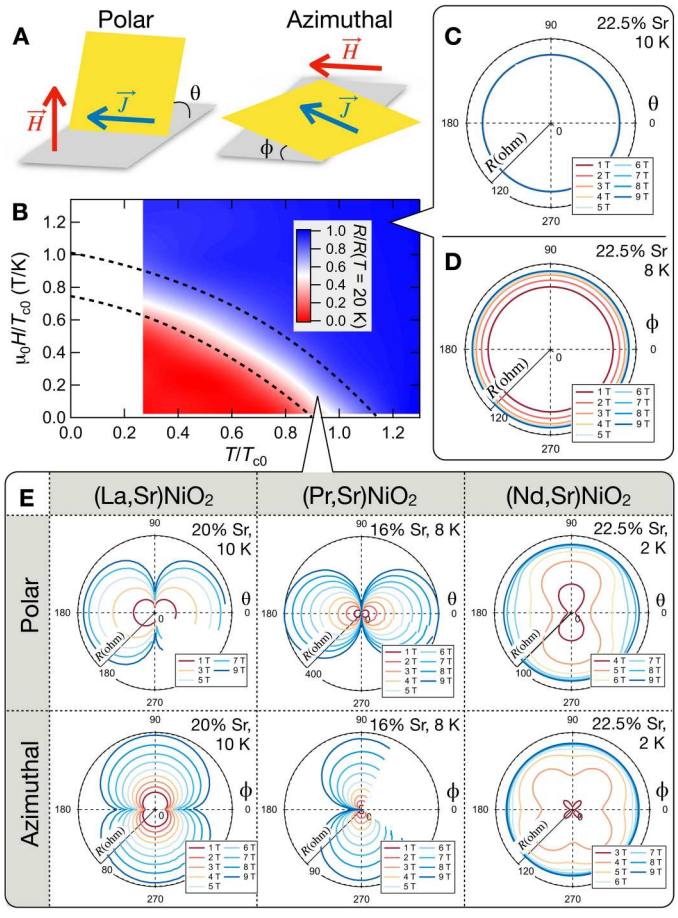

Fig. 2. Representative characteristics of the angular magnetoresistance in (R,Sr)NiO_2. (**A**) Schematic of the measurement geometry with respect to the sample (yellow square). The blue and red arrows represent the directions of the measurement current and the external magnetic field, respectively. (**B**) Magnetic field versus temperature phase diagram of a representative $Nd_{0.775}Sr_{0.225}NiO_2$ sample (T_{c0} = 7.4 K). (**C** and **D**) Representative polar (θ) and azimuthal (ϕ) angle dependence of the magnetoresistance in the normal state for $Nd_{0.775}Sr_{0.225}NiO_2$. (**E**) Representative polar and azimuthal angle dependence of magnetoresistance in the superconducting transition region for La-, Pr-, and Nd-nickelates, with the specific doping and temperature indicated at the top right corner of each panel.

Following these CEF considerations, we can construct a simple model that quantitatively describes all of the angular magnetoresistance data, based on the assumption that the Nd 4*f* moment contributes purely to the background magnetization and magnetic permeability of the lattice. For the θ-dependent magnetoresistance, all the nickelates have in common anisotropic orbital depairing (AOD; Fig. 4A) as a natural consequence of the shorter *c*-axis coherence length (*30*), and hence an $H_{c2||}$ larger than $H_{c2\perp}$. This can be seen to dominate at all temperatures for La-/Pr-nickelates (fig. S3). For Nd-nickelates, there is an additional competing term due to the enhanced magnetic permeability (EMP; Fig. 4B) arising from the 4*f* moments, which has crucially the opposite anisotropy given the easy-plane magnetic anisotropy.

The temperature-dependent balance of this competition (Fig. 4F) underlies the remarkable reversal of the θ-dependent magnetoresistance anisotropy we observe for highly doped Nd-nickelates (Fig. 4G)—i.e., the temperature-dependent crossing of $H_{c2\perp}$ and $H_{c2||}$. Our minimal model is unexpectedly quantitative; the measured magnetoresistance of all samples (La, Pr, and Nd), doping levels, temperatures, and magnetic fields can be described by one generic form for the resistance $R_{AOD}(\theta)$ arising from AOD and another generic form for the resistance $R_{EMP}(\theta)$ from EMP for Nd, such that the total θ-dependent resistance $R^{PL}(\theta)$ can be expressed as

$$R^{PL}(\theta) = C + \alpha_{AOD}R_{AOD}(\theta) + \alpha_{EMP}R_{EMP}(\theta) \quad (1)$$

Here, C, is a constant, and α_{AOD} and α_{EMP} are the temperature- and magnetic field–dependent coefficients of the two functional forms (fig. S8). The dashed lines in Fig. 4G and fig. S4 show the accuracy of this two-component description. In particular, as the polar anisotropy reverses with temperature, the competing AOD and EMP terms produce complex θ-dependences with up to 6 local resistance maxima (fig. S4), which can be well described by Eq. 1.

As for the ϕ-dependent magnetoresistance, we see a competition between a twofold symmetric (C_2) ϕ-dependence and a fourfold symmetric (C_4) ϕ-dependence (Fig. 4D, E, and H). The C_2 response has been seen previously (*32*, *33*) and is a generic result of the ϕ-dependence of the Lorentz force exerted by the measurement current on vortices, because only the perpendicular component contributes. Thus, this ϕ-dependence is seen in all R-variants of the nickelates. However, uniquely in the Nd-nickelates, we observe an additional sin(4ϕ) component (clover-leaf pattern, Fig. 4I), such that the total ϕ-dependent resistance $R^{AZ}(\phi)$ can be then expressed as

$$R^{AZ}(\phi) = C + \alpha_{c2}\sin[2(\phi - \phi_{c2})] + \alpha_{c4}\sin[4(\phi - \phi_{c4})] \quad (2)$$

Here, C, ϕ_{c2}, and ϕ_{c4} are constants, and α_{c2} and α_{c4} are the temperature- and magnetic field–dependent coefficients (figs. S5 and S8). We attribute the C_4 symmetric dependence again to the 4*f* moments, because the occupied CEF levels are necessarily invariant to C_4 symmetry operations. This implies an in-plane magnetic easy axis along the [110] and equivalent directions. This interpretation is bolstered by the experimental observation that ϕ_{c2} follows the applied current direction, while ϕ_{c4} is locked to the lattice (fig. S9).

The extracted coefficients α_{AOD}, α_{EMP}, α_{c2}, and α_{c4} exhibit peaks in magnetic field for a given constant temperature (fig. S8), which is a natural result of the boundary conditions: In either the fully superconducting or normal state, no angle-dependent magnetoresistance is seen. With decreasing temperature, both the peaks in α_{EMP} and α_{AOD} shift to higher magnetic fields, tracing the superconducting phase boundary in the temperature-field plane (Fig. 2B). However, the magnitude of α_{AOD} drops substantially with decreasing temperature, contrasting with the increase in α_{EMP}.

DISCUSSION

The pair-breaking framework of superconductivity is useful to discuss these observations. To leading order, the external magnetic field suppresses superconductivity through either orbital or paramagnetic depairing (*30*). While orbital depairing has an intrinsic θ-dependence rooted in the superconducting anisotropy, paramagnetic depairing is largely isotropic as it suppresses superconductivity by the Zeeman energy cost. Therefore, although both effects are enhanced by the local magnetic field arising from the Nd 4*f*

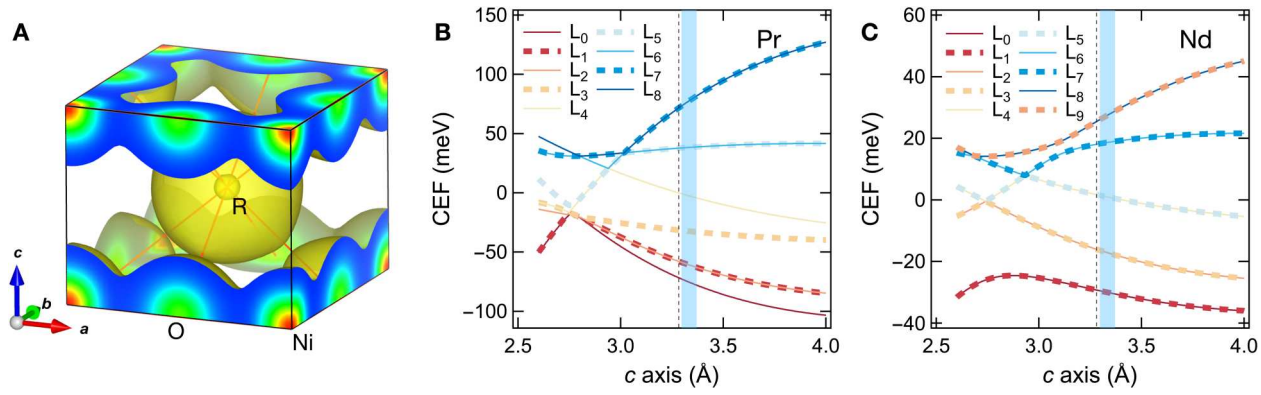

Fig. 3. Calculation of 4*f* CEF levels. (**A**) DFT-calculated electron density distribution of $NdNiO_2$, with the valence including Nd 5*d*, 6*s*, Ni 3*d*, 4*s*, and O 2*p* electrons. The yellow isosurface gives the contour corresponding to 2.5% of the maximum electron density. DFT calculations using a Pr pseudopotential result in a visually indistinguishable charge distribution. (**B** and **C**) Calculated CEF splitting as a function of *c*-axis lattice constant for Pr- and Nd-nickelates, respectively. The blue shaded region marks the range of experimental *c*-lattice constant values, and the vertical dashed line marks the undoped bulk value (*38*). The crystal field levels L_x are expanded in table S1.

moments, an underlying θ-dependence of the local magnetic field intensity is more readily visible when paramagnetic depairing is dominant. With this in mind, we can associate $\alpha_{AOD}R_{AOD}(\theta)$ with orbital depairing, and $\alpha_{EMP}R_{EMP}(\theta)$ with paramagnetic depairing, which dominates at low temperatures.

In contrast, neither depairing effect has intrinsic ϕ-dependence, and both would faithfully exhibit the structure of the local magnetic field. Therefore, the clover-leaf pattern is a direct manifestation of the ϕ-dependence of the local magnetic field intensity, particularly because α_{c4} is consistently an order of magnitude larger than α_{c2} where it is observed (figs. S8 and S10; see the Supplementary Materials for more details on an additional C_2 symmetric response). With decreasing temperature, the onset and marked increase of α_{c4} signal the growing contribution of the 4*f* moments, which in turn enhances α_{EMP}. Note that while the magnetic response of the 4*f* moments likely exists over a broader range of temperature and magnetic field, it only appears in the magnetoresistance in the vicinity of H_{c2} through pair-breaking effects and, in this process, becomes intertwined with the superconducting response. Therefore, the exact temperature or field dependence of the 4*f* magnetic moment magnetization cannot be simply extracted from these data. However, the impact of Nd on H_{c2} is suggestive of low-temperature Nd 4*f* antiferromagnetic exchange, as is typically observed for complex materials hosting magnetic *R*-sites (fig. S11) (*39*).

With these developments, we lastly return to the differences in H_{c2} across *R*-variants shown in Fig. 1. With important 4*f* moment

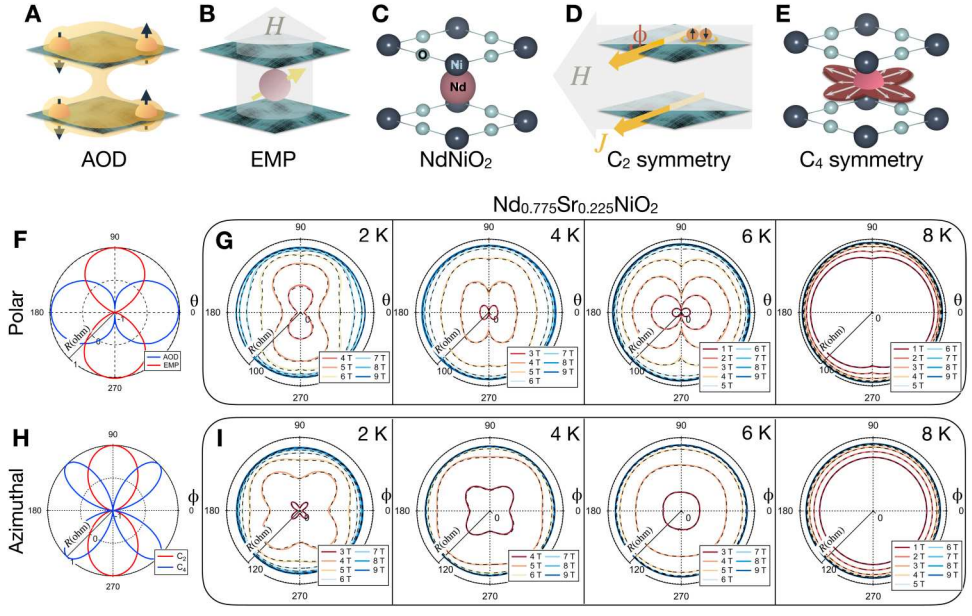

Fig. 4. Competing effects in the angular magnetoresistance. (**A** to **E**) Schematic illustrations of (A) AOD, (B) EMP, and the origin of the (D) C_2 and (E) C_4 symmetric azimuthal response. (C) Corresponding unit cell. (**F** and **H**) Fitting functions corresponding to the AOD and EMP effects for θ-dependence and C_2 and C_4 symmetric ϕ-dependence, respectively. (**G** and **I**) Temperature and magnetic field dependence of the θ- and ϕ-dependence of magnetoresistance of $Nd_{0.775}Sr_{0.225}NiO_2$. Fits based on Eqs. 1 and 2 are shown in black dashed lines.

enhancements of the field, Nd has the lowest H_{c2}/T_{c0}; in their absence, H_{c2}/T_{c0} is highest for La. Pr is intermediate, consistent with the contribution of a Pr^{3+} 4*f* moment induced by magnetic field. Thus, we see that the underlying intrinsic behavior of H_{c2} appears to be similar across the infinite-layer nickelates, once the additional suppression due to the *R*-site magnetism has been taken into account. This leads to the conclusion that the conventional weak-coupling Pauli limit $H_{c2} = 1.86\ T_{c0}$ (*40*) is broadly exceeded, at least with respect to T_{c0}. Although the (Nd,Sr)NiO_2 samples obey this limit (Fig. 1F) (*29*), we now understand this to occur because of Nd 4*f* moment contributions. We observe that the Pauli limit is surpassed by up to a factor of 3.5 in the La series (Fig. 1F). Note that we use a 50% resistance criterion for H_{c2}, to minimize contributions from superconducting fluctuations and vortex creep (*29*); adopting higher resistance thresholds would make this discrepancy even larger.

While the magnitude of H_{c2} presents an important question for future research, we discuss potentially relevant scenarios. We observe that the angular magnetoresistance in the Nd-nickelates can be fully captured by considering only the 4*f* moment contribution to the background magnetization and magnetic permeability. However, it is important to note that this does not preclude other contributions from the hybridization between the *R* 5*d* and the Ni 3*d* orbitals—in the presence of finite spin-orbit coupling, multiorbital mixing could enhance H_{c2}. Perhaps the most straightforward explanation is that the experimentally observed T_{c0} via transport occurs in the presence of substantial phase fluctuations/disorder and does not reflect the pairing scale Δ_0. Tunneling spectroscopy indicates a large Δ_0-to-T_{c0} ratio, although surface effects and variations remain to be clarified (*41*). Further evidence for this scenario may be found in a recent study of $La_{0.8}Sr_{0.2}NiO_2$ with higher T_{c0} but comparable extrapolations of H_{c2} to what we observe (*42*). The fact that experimentally, nickelate superconductivity is in the dirty limit appears to us to disfavor more exotic mean-field enhancements. Independent of origin, the unusually large H_{c2}/T_{c0} ratios in the nickelates, combined with sensitive control through the *R*-site, give properties that would be useful for high-field applications. Provided that substantial further advances can be made in materials synthesis, nickelates could be used for superconducting wires and components, particularly in chemically reducing environments (*43*).

MATERIALS AND METHODS

Materials

Thin-film nickelate samples (7 nm thick) were grown on $SrTiO_3$ substrates using pulsed-laser deposition under growth and reduction conditions previously reported (*1*, *2*, *3*, *44*).

Methods

For angular magnetoresistance measurements, the samples were contacted using wire-bonded aluminum wires in a 6-point Hall bar geometry. The 50% resistive criterion is applied to both temperature-sweep and field-sweep data to determine T_{c0} and H_{c2}. For high-field measurements, transport measurements were performed using the standard four-probe lock-in technique, with an alternating current excitation between 1 and 10 μA. Continuous magnetic fields up to 35 T were generated using a Bitter magnet, coupled with a He-3 cryostat, at the High Field Magnet Laboratory at Nijmegen, the Netherlands. The magnetic field angle was varied in situ using a customized rotator stage.

Note

During the preparation and review of this manuscript, we became aware of two reports on H_{c2} in La-nickelates (*42*, *45*) and three reports on Nd-nickelates (*46*–*48*). All the reported behavior is qualitatively consistent with our results, independent of variations in the magnitude of the resistivity (see also fig. S12), and they further demonstrate that the presence or absence of a capping layer has minimal impact on the observed angular magnetoresistance. We also note that our crystal field assignment for the doped Nd system is very consistent with recent bulk neutron diffraction measurements (*49*).

Supplementary Materials

This PDF file includes:

Supplementary Text
Figs. S1 to S12
Table S1

REFERENCES AND NOTES

1. D. Li, K. Lee, B. Y. Wang, M. Osada, S. Crossley, H. R. Lee, Y. Cui, Y. Hikita, H. Y. Hwang, Superconductivity in an infinite-layer nickelate. *Nature* **572**, 624–627 (2019).
2. M. Osada, B. Y. Wang, K. Lee, D. Li, H. Y. Hwang, Phase diagram of infinite layer praseodymium nickelate $Pr_{1-x}Sr_xNiO_2$ thin films. *Phys. Rev. Mater.* **4**, 121801(R) (2020).
3. M. Osada, B. Y. Wang, B. H. Goodge, S. P. Harvey, K. Lee, D. Li, L. F. Kourkoutis, H. Y. Hwang, Nickelate superconductivity without rare-earth magnetism: (La,Sr)NiO_2. *Adv. Mater.* **33**, 2104083 (2021).
4. S. W. Zeng, C. J. Li, L. E. Chow, Y. Cao, Z. T. Zhang, C. S. Tang, X. M. Yin, Z. S. Lim, J. X. Hu, P. Yang, A. Ariando, Superconductivity in infinite-layer nickelate $La_{1-x}Ca_xNiO_2$ thin films. *Sci. Adv.* **8**, eabl9927 (2022).
5. D. Zhao, Y. B. Zhou, Y. Fu, L. Wang, X. F. Zhou, H. Cheng, J. Li, D. W. Song, S. J. Li, B. L. Kang, L. X. Zheng, L. P. Nie, Z. M. Wu, M. Shan, F. H. Yu, J. J. Ying, S. M. Wang, J. W. Mei, T. Wu, X. H. Chen, Intrinsic spin susceptibility and pseudogaplike behavior in infinite-layer $LaNiO_2$. *Phys. Rev. Lett.* **126**, 197001 (2021).
6. J. Zhang, D. M. Pajerowski, A. S. Botana, H. Zheng, L. Harriger, J. Rodriguez-Rivera, J. P. Ruff, N. J. Schreiber, B. Wang, Y. S. Chen, W. C. Chen, M. R. Norman, S. Rosenkranz, J. F. Mitchell, D. Phelan, Spin stripe order in a square planar trilayer nickelate. *Phys. Rev. Lett.* **122**, 247201 (2019).
7. J. Q. Lin, P. V. Arribi, G. Fabbris, A. S. Botana, D. Meyers, H. Miao, Y. Shen, D. G. Mazzone, J. Feng, S. G. Chiuzbăian, A. Nag, A. C. Walters, M. García-Fernández, J. Ke-Jin Zhou, I. Pelliciari, J. W. Jarrige, J. Z. Freeland, J. F. Mitchell, V. Bisogni, X. Liu, M. R. Norman, M. P. M. Dean, Strong superexchange in a $d^{9-\delta}$ Nickelate revealed by resonant inelastic X-ray scattering. *Phys. Rev. Lett.* **126**, 087001 (2021).
8. G. A. Pan, D. Ferenc Segedin, H. LaBollita, Q. Song, E. M. Nica, B. H. Goodge, A. T. Pierce, S. Doyle, S. Novakov, D. Córdova Carrizales, A. T. N'Diaye, P. Shafer, H. Paik, J. T. Heron, J. A. Mason, A. Yacoby, L. F. Kourkoutis, O. Erten, C. M. Brooks, A. S. Botana, J. A. Mundy, Superconductivity in a quintuple-layer square-planar nickelate. *Nat. Mater.* **21**, 160–164 (2022).
9. M. F. Hundley, J. D. Thompson, S.-W. Cheong, Z. Fisk, S. B. Oseroff, Specific heat and anisotropic magnetic susceptibility of Pr_2CuO_4, Nd_2CuO_4 and Sm_2CuO_4 crystals. *Phys. C Supercond.* **158**, 102–108 (1989).
10. J. W. Lynn, I. W. Sumarlin, S. Skanthakumar, W.-H. Li, R. N. Shelton, J. L. Peng, Z. Fisk, S.-W. Cheong, Magnetic ordering of Nd in $(Nd,Ce)_2CuO_4$. *Phys. Rev. B* **41**, 2569–2572 (1990).
11. R. Fehrenbacher, T. M. Rice, Unusual electronic structure of $PrBa2Cu_3O_7$. *Phys. Rev. Lett.* **70**, 3471–3474 (1993).
12. M. R. Norman, Entering the nickel age of superconductivity. *Phys. Ther.* **13**, 85 (2020).
13. W. E. Pickett, The dawn of the nickel age of superconductivity. *Nat. Rev. Phys.* **3**, 7–8 (2021).
14. A. S. Botana, F. Bernardini, A. Cano, Nickelate superconductors: An ongoing dialog between theory and experiments. *J. Exp. Theor. Phys.* **132**, 618–627 (2021).
15. Y. Nomura, R. Arita, Superconductivity in infinite-layer nickelates. *Rep. Prog. Phys.* **85**, 052501 (2022).
16. F. Lechermann, Late transition metal oxides with infinite-layer structure: Nickelates versus cuprates. *Phys. Rev. B* **101**, 081110 (2020).

17. D. Li, B. Y. Wang, K. Lee, S. P. Harvey, M. Osada, B. H. Goodge, L. F. Kourkoutis, H. Y. Hwang, Superconducting dome in $Nd_{1-x}Sr_xNiO_2$ infinite layer films. *Phys. Rev. Lett.* **125**, 027001 (2020).
18. S. Zeng, C. S. Tang, X. Yin, C. Li, M. Li, Z. Huang, J. Hu, W. Liu, G. J. Omar, H. Jani, Z. S. Lim, K. Han, D. Wan, P. Yang, S. J. Pennycook, A. T. S. Wee, A. Ariando, Phase diagram and superconducting dome of infinite-layer $Nd_{1-x}Sr_xNiO_2$ thin films. *Phys. Rev. Lett.* **125**, 147003 (2020).
19. Y. Xiang, Q. Li, Y. Li, H. Yang, N. Feng, H. -H. Wen, Physical properties revealed by transport measurements for superconducting $Nd_{0.8}Sr_{0.2}NiO_2$ thin films. *Chin. Phys. Lett.* **38**, 047401 (2021).
20. Y. -T. Hsu, B. Y. Wang, M. Berben, D. Li, K. Lee, C. Duffy, T. Ottenbros, W. J. Kim, M. Osada, S. Wiedmann, H. Y. Hwang, N. E. Hussey, Insulator-to-metal crossover near the edge of the superconducting dome in $Nd_{1-x}Sr_xNiO_2$. *Phys. Rev. Res.* **3**, L042015 (2021).
21. N. N. Wang, M. W. Yang, Z. Yang, K. Y. Chen, H. Zhang, Q. H. Zhang, Z. H. Zhu, Y. Uwatoko, L. Gu, X. L. Dong, J. P. Sun, K. J. Jin, J.-G. Cheng, Pressure-induced monotonic enhancement of T_c to over 30 K in superconducting $Pr_{0.82}Sr_{0.18}NiO_2$ thin films. *Nat. Commun.* **13**, 4367 (2022).
22. M. Hepting, M. P. M. Dean, W. S. Lee, Soft X-ray spectroscopy of low-valence nickelates. *Front. Phys.* **9**, 808683 (2021).
23. B. H. Goodge, D. Li, K. Lee, M. Osada, B. Y. Wang, G. A. Sawatzky, H. Y. Hwang, L. F. Kourkoutis, Doping evolution of the Mott–Hubbard landscape in infinite-layer nickelates. *Proc. Natl. Acad. Sci. U.S.A.* **118**, e2007683118 (2021).
24. M. Rossi, H. Lu, A. Nag, D. Li, M. Osada, K. Lee, B. Y. Wang, S. Agrestini, M. Garcia-Fernandez, J. J. Kas, Y.-D. Chuang, Z. X. Shen, H. Y. Hwang, B. Moritz, K.-J. Zhou, T. P. Devereaux, W. S. Lee, Orbital and spin character of doped carriers in infinite-layer nickelates. *Phys. Rev. B* **104**, L220505 (2021).
25. P. Jiang, L. Si, Z. Liao, Z. Zhong, Electronic structure of rare-earth infinite-layer $RNiO_2$ (R = La, Nd). *Phys. Rev. B* **100**, 201106 (2019).
26. S. Bandyopadhyay, P. Adhikary, T. Das, I. Dasgupta, T. Saha-Dasgupta, Superconductivity in infinite-layer nickelates: Role of *f* orbitals. *Phys. Rev. B* **102**, 220502 (2020).
27. M. -Y. Choi, K. -W. Lee, W. E. Pickett, Role of 4 *f* states in infinite-layer $NdNiO_2$. *Phys. Rev. B* **101**, 020503 (2020).
28. R. Zhang, C. Lane, B. Singh, J. Nokelainen, B. Barbiellini, R. S. Markiewicz, A. Bansil, J. Sun, Magnetic and *f*-electron effects in $LaNiO_2$ and $NdNiO_2$ nickelates with cuprate-like $3d_{x^2-y^2}$ band. *Commun. Phys.* **4**, 118 (2021).
29. B. Y. Wang, D. Li, B. H. Goodge, K. Lee, M. Osada, S. P. Harvey, L. F. Kourkoutis, M. R. Beasley, H. Y. Hwang, Isotropic Pauli-limited superconductivity in the infinite-layer nickelate $Nd_{0.775}Sr_{0.225}NiO_2$. *Nat. Phys.* **17**, 473–477 (2021).
30. M. Tinkham, *Introduction to Superconductivity* (McGraw-Hill Inc., ed. 2, 1996).
31. K. Maki, T. Tsuneto, Pauli paramagnetism and superconducting state. *Prog. Theor. Phys.* **31**, 945–956 (1964).
32. Y. Iye, A. Fukushima, T. Tamegai, T. Terashima, Y. Bando, Anisotropy and dissipation in the mixed state of high temperature superconductors. *Phys. C Supercond.* **185**–**189**, 297–302 (1991).
33. Y. Iye, A. Watanabe, S. Nakamura, T. Tamegai, T. Terashima, K. Yamamoto, Y. Bando, Dissipation in the mixed state of conventional and high temperature superconductors. *Phys. C Supercond.* **167**, 278–286 (1990).
34. A. A. B. Baloch, S. M. Alqahtani, F. Mumtaz, A. H. Muqaibel, S. N. Rashkeev, F. H. Alharbi, Extending Shannon's ionic radii database using machine learning. *Phys. Rev. Mater.* **5**, 043804 (2021).
35. J. P. Perdew, K. Burke, M. Ernzerhof, Generalized gradient approximation made simple. *Phys. Rev. Lett.* **77**, 3865–3868 (1996).
36. G. Kresse, J. Hafner, Ab initio molecular dynamics for liquid metals. *Phys. Rev. B* **47**, 558–561 (1993).
37. W. Tang, E. Sanville, G. Henkelman, A grid-based Bader analysis algorithm without lattice bias. *J. Phys. Condens. Matter* **21**, 084204 (2009).
38. H. Lin, D. J. Gawryluk, Y. M. Klein, S. Huangfu, E. Pomjakushina, F. von Rohr, A. Schilling, Universal spin-glass behaviour in bulk $LaNiO_2$, $PrNiO_2$ and $NdNiO_2$. *New J. Phys.* **24**, 013022 (2022).
39. A. I. Buzdin, L. N. Bulaevskiĭ, Antiferromagnetic superconductors. *Sov. Phys. Uspekhi* **29**, 412–425 (1986).
40. A. M. Clogston, Upper limit for the critical field in hard superconductors. *Phys. Rev. Lett.* **9**, 266–267 (1962).
41. Q. Gu, Y. Li, S. Wan, H. Li, W. Guo, H. Yang, Q. Li, X. Zhu, X. Pan, Y. Nie, H. -H. Wen, Single particle tunneling spectrum of superconducting $Nd_{1-x}Sr_xNiO_2$ thin films. *Nat. Commun.* **11**, 6027 (2020).
42. W. Sun, Y. Li, R. Liu, J. Yang, J. Li, S. Yan, H. Sun, W. Guo, Z. Gu, Y. Deng, X. Wang, Y. Nie, Evidence for quasi-two-dimensional superconductivity in infinite-layer nickelates. arXiv:2204.13264 [cond-mat.supr-con] (28 April 2022).
43. X. Xu, A review and prospects for Nb_3Sn superconductor development. *Supercond. Sci. Tech.* **30**, 093001 (2017).
44. K. Lee, B. H. Goodge, D. Li, M. Osada, B. Y. Wang, Y. Cui, L. F. Kourkoutis, H. Y. Hwang, Aspects of the synthesis of thin film superconducting infinite-layer nickelates. *APL Mater.* **8**, 041107 (2020).
45. L. E. Chow, K. Y. Yip, M. Pierre, S. W. Zeng, Z. T. Zhang, T. Heil, J. Deuschle, P. Nandi, S. K. Sudheesh, Z. S. Lim, Z. Y. Luo, M. Nardone, A. Zitouni, P. A. van Aken, M. Goiran, S. K. Goh, W. Escoffier, A. Ariando, Pauli-limit violation in lanthanide infinite-layer nickelate superconductors. arXiv:2204.12606 [cond-mat.supr-con] (26 April 2022).
46. G. Krieger, A. Raji, L. Schlur, G. Versini, C. Bouillet, M. Lenertz, J. Robert, A. Gloter, N. Viart, D. Preziosi, Synthesis of infinite-layer nickelates and influence of the capping-layer on magnetotransport. *J. Phys. D App. Phys.* **56**, 024003 (2022).
47. H. Ji, Y. Li, Y. Liu, X. Ding, Z. Xie, S. Qi, L. Qiao, Y. Yang, G.-M. Zhang, J. Wang, Rotational symmetry breaking in superconducting nickelate $Nd_{0.8}Sr_{0.2}NiO_2$ films. arXiv:2210.17023. [cond-mat.supr-con] (31 October 2022).
48. L. E. Chow, K. Rubi, K. Y. Yip, M. Pierre, M. Leroux, X. Liu, Z. Luo, S. Zeng, C. Li, M. Goiran, N. Harrison, W. Escoffier, S. K. Goh, A. Ariando, Dimensionality control and rotational symmetry breaking superconductivity in square-planar layered nickelates. arXiv:2301.07606 [cond-mat.supr-con] (18 January 2023).
49. S. Rosenkranz, D. Phelan, B. Wang, H. Zheng, D. L. Abernathy, A. S. Botana, J. F. Mitchell, Inelastic neutron scattering study of the infinite layer nickelate $Nd_{0.8}Sr_{0.2}NiO_2$. Bull. Am. Phys. Soc., (2023). https://meetings.aps.org/Meeting/MAR23/Session/S19.10
50. J. A. Smith, M. J. Cima, N. Sonnenberg, High critical current density thick MOD-derived YBCO films. *IEEE Trans. Appl. Supercond.* **9**, 1531–1534 (1999).
51. M. T. Hutchings, Point-charge calculations of energy levels of magnetic ions in crystalline electric field, in *Solid State Physics*, F. Seitz, D. Turnbull, Eds. (Elsevier Amsterdam, 1964), vol. 16, pp. 227–273.
52. M. Yu, D. R. Trinkle, Accurate and efficient algorithm for Bader charge integration. *J. Chem. Phys.* **134**, 064111 (2011).
53. A. Gelessus, W. Thiel, W. Weber, Multipoles and symmetry. *J. Chem. Educ.* **72**, 505–508 (1995).
54. K. Lee, B. Y. Wang, M. Osada, B. H. Goodge, T. C. Wang, Y. Lee, S. Harvey, W. J. Kim, Y. Yu, C. Murthy, S. Raghu, L. F. Kourkoutis, H. Y. Hwang, Character of the "normal state" of the nickelate superconductors. arXiv:2203.02580v1 [cond-mat.supr-con] (4 March 2022).

Acknowledgments: We thank S. A. Kivelson, C. Murthy, S. Raghu, and Y. Yu for fruitful discussions and Y. Yu and S. P. Harvey for critical reading of the manuscript. We acknowledge the support of the HFML-RU/NWO, a member of the European Magnetic Field Laboratory (EMFL). IRB and/or IACUC guidelines were followed with human or animal subjects. **Funding:** This work was supported by the US Department of Energy, Office of Basic Energy Sciences, Division of Materials Sciences and Engineering grant DE-AC02-76SF00515 (to B.Y.W., T.C.W., M.O., K.L., C.J., D.L., T.P.D., I.R.F., and H.Y.H.); Gordon and Betty Moore Foundation's Emergent Phenomena in Quantum Systems Initiative grant GBMF9072 (to J.F. and H.Y.H.); the Swiss National Science Foundation through Postdoc.Mobility P400P2199297 (to J.F.); and the European Research Council (ERC) under the European Union's Horizon 2020 research and innovation program (grant agreement no. 835279-Catch-22) (to Y.-T.H., C.D., and N.E.H.). **Author contributions:** Conceptualization: B.Y.W. and H.Y.H. Sample synthesis: M.O., K.L., D.L., and J.F. Transport characterization: B.Y.W., T.C.W., Y.-T.H., and C.D. Theoretical calculation: B.Y.W. and C.J. Funding acquisition: H.Y.H., T.P.D., and N.E.H. Supervision: M.R.B., T.P.D., N.E.H., I.R.F., and H.Y.H. Writing: B.Y.W., T.C.W., and H.Y.H. **Competing interests:** The authors declare that they have no competing interests. **Data and materials availability:** All data needed to evaluate the conclusions in the paper are present in the paper and/or the Supplementary Materials.

Submitted 5 November 2022
Accepted 14 April 2023
Published 17 May 2023
10.1126/sciadv.adf6655